designs

MDPI

Article

By Visualizing the Deformation with Mechanoluminescent Particles, Additive Manufacturing Offers a Practical Alternative to Stress and Strain Simulation

Ernests Einbergs *, Agnese Spustaka, Virginija Vitola and Aleksejs Zolotarjovs

Institute of Solid State Physics, University of Latvia, Kengaraga Str. 8, LV 1063 Riga, Latvia
* Correspondence: ernests.einbergs@cfi.lu.lv

Abstract: The use of stress–strain analysis in structural design or mechanical components is critical for avoiding or investigating structural failures. In the case of complicated designs, mathematical full-field stress modeling produces imprecise predictions. Experimental analysis can be used as a replacement for mathematical modeling, but with the use of currently available strain gauges, it is cumbersome and impossible in the case of moving parts. Mechanoluminescent materials transform mechanical energy into visible light and can be used as a replacement for strain gauges to monitor strain/stress. Three-dimensional printing technology has made major advances in terms of additive manufacturing. In this article, we describe a method to produce an ML 3D print. The fabricated samples are precise and versatile and satisfy the need for easy and non-destructible spatial stress analysis. A 3D printed photopolymer sample with $SrAl_2O_4$: Eu, Dy particle addition only to the final layers was tested, and the number of layers was optimized. It was determined that the optimal number of layers for easy detection is in the range of 10 to 20 layers. It opens the possibility for the real-time evaluation of complex uneven forces on complex parts, thus having a good potential for commercialization.

Keywords: mechanoluminescence; additive manufacturing; 3D printing; stress analysis; mechanical components; non-destructive; full-field strain measurements

Citation: Einbergs, E.; Spustaka, A.; Vitola, V.; Zolotarjovs, A. By Visualizing the Deformation with Mechanoluminescent Particles, Additive Manufacturing Offers a Practical Alternative to Stress and Strain Simulation. *Designs* **2023**, *7*, 54. https://doi.org/10.3390/designs7020054

Academic Editor: Ali Zolfagharian

Received: 1 March 2023
Revised: 31 March 2023
Accepted: 4 April 2023
Published: 7 April 2023

1. Introduction

Three-dimensional printing technology is an additive manufacturing technique for producing a variety of complex structures from three-dimensional models. Manufacturing and logistics operations can be improved by 3D printing, which has evolved over the years and includes a wide range of methods, materials, and tools. In recent years, it has made significant advancements, as the expiration of earlier patents, which allowed manufacturers to create new 3D printing devices, is one of the key factors contributing to this technology's accessibility. Recent innovations have decreased the price of 3D printers, extending their use in laboratories, schools, and homes. The technology has enabled the production of functional prototypes, lightweight components, and customized tools, among other things. New applications are constantly appearing as a result of the constant development of cutting-edge materials and additive manufacturing techniques, significantly advancing a number of industries, including engineering and healthcare [1–3]. A need for specialized stress sensors has also arisen from the use of stimulus-responsive materials in 3D printing, where printed objects can change shape or qualities in reaction to external stimuli, such as heat [4], light [5], electricity [6], magnetism [7], water [8], mechanical stress, etc. Stress, pressure, and capacitive touch sensing have already been extensively used in a variety of fields, ranging from mobile phones to electronic touch screens, automobiles, and aircraft.

Mechanoluminescence (ML) is the non-thermal emission of light when a material is subjected to stress; thus, ML materials are capable of transforming mechanical energy into visible light [9,10]. This method of strain/stress monitoring with ML materials is currently

under development, and the intensity of ML exhibits a strong correlation with the applied stress, making it suitable for stress sensing and even mapping the stress distribution.

ML materials have been studied for their potential use in various applications, including stress sensing, damage detection, and structural health monitoring [11–15]. They have been used in the development of smart materials, such as self-healing materials and sensors for detecting structural changes in buildings, bridges, and other structures. The method of active strain/stress monitoring with ML materials is currently being developed [16,17]. ML layers are a powerful addition to 3D prototyping, coupled with an optical sensor that can be used as a real-time stress sensor in a 3D-printed part.

While numerical analysis, such as that performed with COMSOL, can provide a simulated approach to stress distribution in parts [18,19], there are often significant differences between a computer model and an experiment that can be created by effects that are unaccounted for, such as sample warping during printing. This can lead to imprecise results, and the extensive testing of parts is usually required before they can be implemented in final assemblies. Conventional stress sensors, such as piezoresistive stress sensors, are commonly used for this purpose. However, they are not always suitable, particularly in cases where the part is in motion, such as rotating gear. Furthermore, conventional stress sensors only provide information about the stress at the point, line, or interface where the sensor is applied, and do not provide a full picture of the stress distribution within the mechanical part. Therefore, alternative methods of stress sensing have been sought. The incorporation of mechanoluminescent layers into 3D-printed parts, along with an optical sensor, offers a promising solution for real-time stress sensing and mapping in 3D-printed parts. This technology provides a non-destructive method for detecting stress in various parts of a complex design, including moving parts, and can offer valuable insights into the stress distribution within the printed structure.

This article explores the possibility of adding ML powder ($SrAl_2O_4$: Eu, Dy) to the final layers of a 3D-printed mechanical part, along with a method for real-time stress mapping in the printed part. The number of layers with ML particles that are most efficient is deduced in terms of the ML intensity and the spatial resolution. This research has the potential to advance the field of 3D printing and provide valuable insights into the stress distribution of printed structures.

2. Materials and Methods

While calculating the stress–strain analysis in uniform, elementary objects are relatively simple, obtaining an analytical solution for more complicated geometric shapes becomes difficult. Our method is preferred for determining structural weak points in components with non-uniform stress distribution. A model was developed with the goal of generating non-linear stress distribution during deflection. A dog-bone similar shape was chosen with the dimensions of 100 × 30 × 7 mm. The center is 12 mm wide, a spline function is employed to form the desired shape, and 3 circular cutouts (radius of 5 mm) are added to create structural weaknesses. The aforementioned shape is shown in Figure 1. Large cutouts at both ends of the designed shape serve no purpose other than reducing the overall amount of photopolymer used during LCD stereolithography.

The model was created with Fusion 360 and sliced with Chitubox v1.9.4. The printing parameters were as follows: layer height of 0.01 mm, bottom exposure of 20 s, exposure of 5 s, movement speed of 110 mm/s, lift distance of 5 mm, and rest time of 5 s. It is important to keep the layer height low while printing with a polymer and ML particle mixture, as the particles absorb a considerable part of UV illumination. Overall movement speed was irrelevant, but a pause (rest time) between layers had to be implemented due to the mixture having a higher viscosity than a pure photopolymer and taking longer to fill the void left by the previous layer.

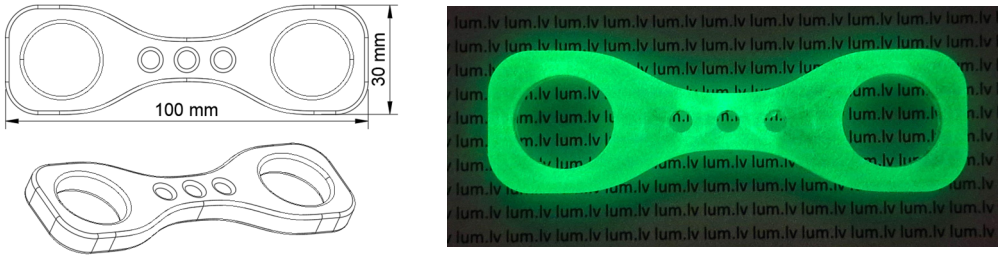

(**a**) (**b**)

Figure 1. (**a**) Used dog-bone-like design as seen in Fusion360; (**b**) sample with 20 luminescent layers 30 s after UV excitation.

Multiple research groups have extensively examined strontium aluminate [12,16,20,21], which is among the most studied materials with long-lasting and predictable, repeatable afterglow and ML properties. Therefore, this material was chosen as the ML powder for this research. Prints were made with a conventional and affordable stereolithography (SLA) printer Elegoo Mars 2 Pro. Before application, the polymer and ML powder mixture was stirred with Heathrow Scientific Vortex for 30 min, after which it was poured into the reservoir. Transparent ABS-like photopolymer purchased from the printer's manufacturer Elegoo was mixed with monoclinic $SrAl_2O_4$ powder (purchased from Sigma Aldrich) activated with 1 at% Eu^{2+} and 2 at% Dy^{3+} at a ratio of 20 to 1. A preliminary study was performed that determined that the ratio produces samples reliably without meaningful surface defects. Considerably higher concentrations do not suspend for long enough within the photopolymer during printing and settle faster than is desirable. The bulk of the sample was printed with pure photopolymer because, during a bending flexural test, only the outermost layers are subjected to stress. The inner structural layers can be pure photopolymer for cost-saving purposes. For the final N layers (2, 5, 10, 20, 30), the holding vat was removed, cleansed with pure ethanol, and filled with the polymer and ML particle mixture, resulting in a 0.02–0.30 mm thick ML layer. For samples that were meant to contain more than 5 layers of the luminescent material, the print was paused every 5 successful layers and stirred to facilitate the highest achievable particle distribution homogeneity. If the sample displayed any surface defects or fractures during the rest time of the print, the procedure was stopped and restarted from the beginning.

A custom-built measurement apparatus that is capable of deformation and the collection of the emitted light and can provide the precise measurement of displacement, the load applied to the sample as well as the sensitivity to light was employed to measure ML. The setup and working principles of this system are described in detail in [22]. The system is designed around a leadscrew-driven cart system. Three-point flexural tests [23] were performed with the aid of a Nema 23 stepper motor coupled with a 1 to 10 planetary gear set to amplify the force generated. An SFU2005 ballscrew is connected to the gearset shaft with a rigid coupler. A 3D-printed mount connects the ball-bearing cart and the screw nut on the lead screw. The mount is equipped with a load pin with a diameter of 15 mm and a height of 30 mm. The constructed system moves with an accuracy of 6 ± 2 µm per step. Measurements were performed by capturing 16-bit pixel depth images with CMOS Blackfly BFLY–U3–23S6N camera at 2 fps (frames per second) with all built-in image processing functions disabled. Although the camera supports up to 41 fps, a higher framerate is undesirable due to the decrease in the dynamic range under low light conditions and decreased signal-to-noise ratio with the built-in amplifier enabled. Samples were excited for 60 s with a wide spectrum UV light source (450 nm peak).

3. Results

Both afterglow and ML exhibit the same emission spectrum, indicating that Eu^{2+} is the luminescence center involved in both temperature and stress-induced recombination. The emission spectrum of the material is a typical Eu^{2+} emission spectrum [16,24–26]—broad

emission band with a maximum at 530 nm (green light) under UV excitation arising from the luminescent $4f^6 5d \rightarrow 4f^7$ transition. The Eu^{2+} luminescence centers are involved in both temperature and stress-induced recombination because both the afterglow and mechanoluminescence have the same spectrum. The sample exhibits afterglow that is comprised of two components—fast decay and slow decay. The afterglow is very predictable in the same circumstances (mainly temperature). The fast decay arises from charge carrier thermal release from the trapping centers, and the slow decay arises from the emptying of the energetically deeper trapping centers booth by thermal energy and the tunneling of the charge carriers (electrons) to the luminescence center; it is believed that it might also be the mechanism that is responsible for the observed ML during deformation [12,20,27–30] because the probability of tunneling is distance dependent.

A delay between the sample illumination and spatial intensity acquisition was implemented to avoid over-exposure of the CMOS camera during intensive afterglow [21]. The fast component of Eu^{2+} center decay has a significantly higher intensity than that of ML observed during deformation, and it became hard to distinguish ML from the background signal. Therefore, measurements were initiated 3 min after the end of UV irradiation. A shorter delay will yield a lessened ML signal when corrected by subtracting the background signal (further contrast), and a longer delay will make the ML signal more distinguishable at the expense of overall signal intensity.

Luminescence intensity was recorded during one loading-unloading cycle. A region of interest was cut out of the acquired images spanning the length and width of the sample and was integrated to display the change in luminescence intensity. Figure 2a shows the light emission increase as a result of applied stress; for illustrative purposes, afterglow emission was subtracted to highlight the ML. Figure 2b shows the corrected signal and deflection of the sample. High response to even small deformations (starting from 1.6 mm deflection) was observed. No plastic deformation was observed in the range of deflections used. The resulting increase in luminescence emission is clearly distinguishable and visible.

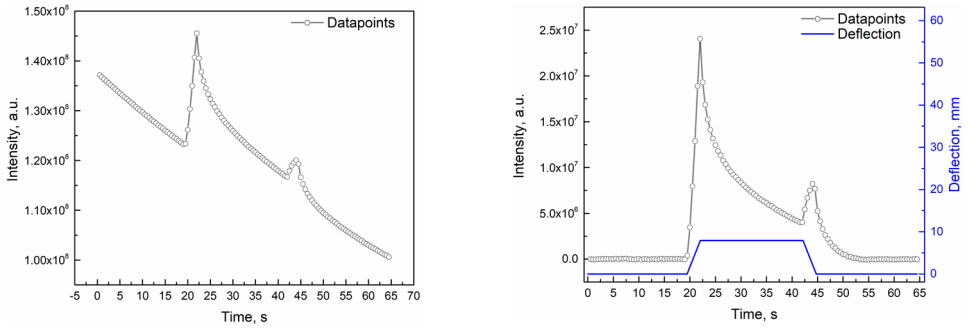

(**a**) (**b**)

Figure 2. (**a**) Integral luminescent emission in one loading–unloading cycle of the 3D-printed sample with 10 luminescent layers; (**b**) deflection of sample and illustration of ML without background afterglow of $SrAl_2O_4$: Eu, Dy.

The measurement error was estimated by repeatedly performing the same measurement under identical conditions. To evaluate measurement repeatability, samples were deformed by 6 mm in an identical experimental environment. It was assumed that the degradation of the photopolymer is statistically insignificant for a population of 10 measurements and the expected value is constant. As no operator input was necessary during repeated tests, it was assumed that the deviation from the average value directly represents the inconsistency of the system itself. The residual from the calculated average contrast is shown in Figure 3. The coefficient of variation was determined to be 4.98%. It was assumed that the overall error of the constructed system would not exceed 10% of the absolute measured value and was added to Figures 4 and 5.

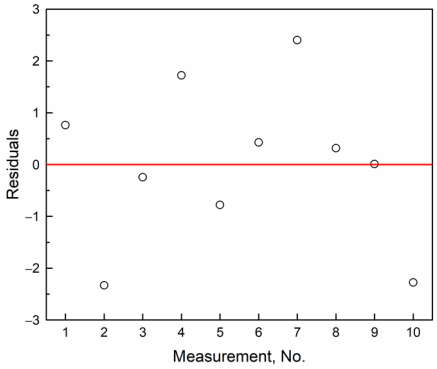

Figure 3. The estimation of the contrast measurement error is 4.98%, based on calculating the relative standard deviation after numerous repetitions of a single loading–unloading cycle.

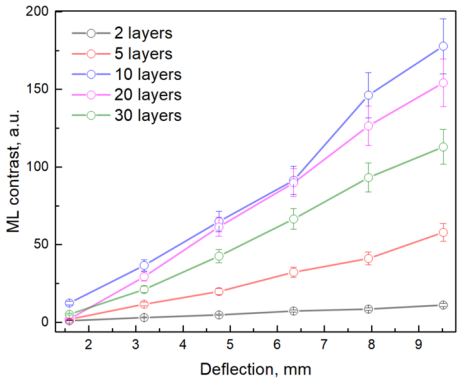

Figure 4. Contrast of ML for samples with N (2, 5, 10, 20, 30) layers changing maximum deflection with an upper estimate of the measurement error of 10%.

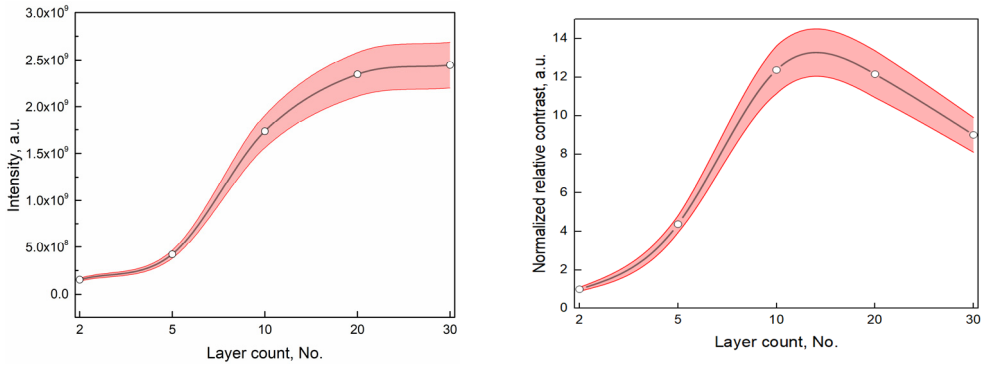

Figure 5. (**a**) The integral luminescence intensity of 3D-printed samples with different counts of ML layers; (**b**) the normalized contrast for 8 mm deflection; points are connected with a spline function for illustrative purposes; the red region represents the estimated 10% error.

For rapid development purposes, it is important to determine the optimal number of layers for stress distribution visualization. Since ML additives are multiple times more expensive compared to photopolymers, a cost-saving measure was implemented, where only the outer layers during a 3D print are filled with ML particles. There are several reasons as to why this was deemed not to impact the final result. The layers that are closer to the neutral axis are subjected to smaller strain and in turn, their contribution to the overall ML signal is proportionally smaller. As the particles will settle eventually, fewer layers will require less interruption of the print procedure and manual mixing. Therefore, a few layers close to the surface of the sample will provide the highest contrast due to being as far from

the neutral axis as possible, but due to the absence of luminescent material, the amount of light emitted during ML is harder to perceive and distinguish from the background signal. During the determination of the optimal number of layers, the contrast was calculated by subtracting the afterglow intensity from the peak observed during deflection. Results are shown in Figure 4. Samples were not mutually normalized to focus on the easiest-to-detect ML signal. If measurements are normalized, the highest contrast is observed for the samples with a smaller amount of ML layers, but it requires a sensitive registration device, which would prove to be inaccurate if less sensitive equipment is used. Figure 5 displays the difference between overall intensity and the determined contrast during ML.

From experimental observations, the highest cost performance is achieved by implementing no fewer than 10 surface layers printed from a mixture of $SrAl_2O_4$: Eu, Dy and photopolymer at a ratio of 1:20. Samples containing 10 luminescent layers displayed almost the same ML contrast as the sample with 20 layers, though slightly higher, but it can be disregarded within the determined margin of error. Samples with 5 and 2 layers have drastically weaker overall luminescence intensity, and the contrast decreases around 3 times when compared to the achievable luminescence with 10 and 20 layers. The sample with 30 layers has the brightest afterglow and, as mentioned previously, has a reduced contrast due to the elevated baseline from layers weakly contributing to the effect of ML. Due to the relatively high cost of ML powder and the fact that the ML signal is strong enough to be noticeable, using fewer than 10 layers of the ML powder and photopolymer mixture is feasible.

The main point of interest in this research, however, is not the integral ML intensities response to strain, as that was already proven as an indication of deformation amplitude by other researchers. Here, we set the main focus on the spatial real-time visualization of mechanical stress. Spatial stress distribution can be deduced in real time by employing the same method described in one of our previous works [23]. For samples with a low contrast, it is possible to rely on the linearity of ML. When a sample is subjected to a constant stress gradient (deformed with constant speed), the rise in intensity is linear, which is observable in Figure 2b as well as in the research by other groups [12,16,24]. By taking each pixel of the image or a region of interest and performing a linear fit over time, the slope in the linear regression formula represents the intensity change during deformation. A simpler approach can be employed in cases with high contrast. ML is a form of stimulated luminescence; any photon released during mechanical interaction is produced at the expense of afterglow. By observing the change in light intensity between a frame during deflection and the beginning of the fast decay right after the end of mechanical interaction, depleted regions can be observed. Due to the fact that ML intensity is related to the absolute stress to which the sample is subjected, it is reasonable to anticipate that the depleted regions are directly linked to surface regions subjected to higher stress. Figure 6a shows the described difference in registered light intensity by subtracting the two frames. Minor image inconsistency is expected due to the reflective surface of the load pin. Figure 6b shows the theoretically calculated von Mises stress distribution. The calculated values are not applicable to the printed samples and are not provided since distribution is geometry related and the absolute value is dependent on the material property.

The distribution that was theoretically calculated and the obtained image match well. Theoretical calculations were performed with COMSOL Multiphysics. The geometry used for calculations was imported from the same file used for the 3D printing of the samples. To minimize the degrees of freedom, a number of simplifications were introduced. It is impossible to create a true-to-life model with no limitations since the calculation will never converge. The supporting pins were considered to be rigid bodies that could be replaced by a fixed-end constraint. The loading pin was modeled as an ideal rigid cylinder. The sample consists of layers. The anisotropic mechanical properties were ignored, and the sample was assumed to be isotropic. The surface layers are a composite structure with anisotropic properties, which may be dependent on print parameters. The resolution of acquired frames was reduced to decrease the noise of the image. The reduction was performed by

adding together values of 9 pixels arranged in a 3 by 3 square region. If further resolution reduction was applied, the overall image noise would decrease, but the surface features of the sample would become harder to distinguish. If a good print can be achieved with an ML particle-to-polymer ratio higher than 1:20, it would lower the image noise and the number of layers necessary to estimate surface stress distribution.

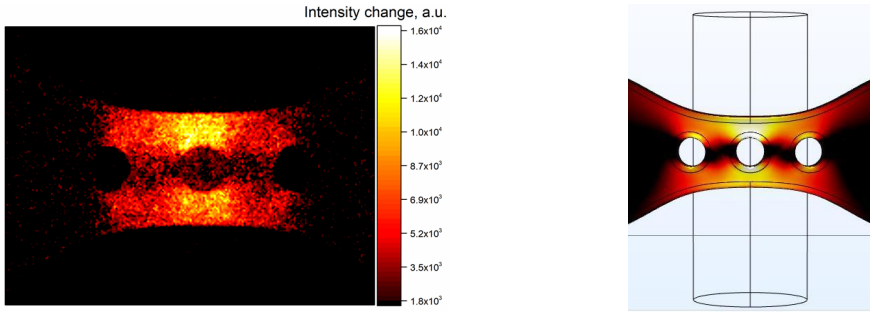

(**a**) (**b**)

Figure 6. (**a**) Obtained image after subtracting two consecutive frames; (**b**) numerical model of stress distribution.

4. Discussion

A novel method for visualizing structural weak points is tested and proven to be viable. The additive manufacture of ML scaled-down models in rapid development settings could provide unforeseen benefits. Three-dimensional printing of a prototype design and its observation with a camera is incomparably faster than performing theoretical calculations with the same accuracy required for a reasonable conclusion. The experimentally acquired stress distribution map is comparable to theoretically calculated models and encourages further methods' refinement for applications in practical circumstances. Further studies should focus on optimizing the ratio between photopolymer and ML material. The most effective excitation required for $SrAl_2O_4$: Eu, Dy luminescence is within the same spectral range as the photopolymer hardening; therefore, complementary research might determine the deterioration of the photopolymer. In the scope of this investigation, no meaningful change in mechanical properties was observed for the tested samples.

To make stress visualization with additive manufacturing more compelling for industrial applications, a combination of ML particles and polymers could be sought. Long-term UV exposure might cause the current combination to degrade, and ML particles further from the surface layers might not be excited and consecutively would not contribute to the observable ML.

Discrepancies between theoretical calculations and empirical observations might be caused by anisotropic mechanical properties. In Figure 6b, the local maxima in the von Mises stress can be observed around the outermost circular cutouts. The absence of intensity change in Figure 6a might be caused by the nonlinear force transfer between the layers and the fact that the layers observed have ceramic particles embedded. The observation of ML implies that either the polymer has adhered to the particles or a strong enough compressive force acts upon them.

Theoretical calculations were performed with the finite element method. This study focuses on von Mises stress. Similar research in the field has shown that a correlation between ML and maximal tensile stress and shear stress exists [12]. The von Mises stress is a measure of the equivalent stress in a material, taking into account tensile and shear stresses. While principal stress could be used as well, as it displays the stress component acting along the principal axis, it is a measure of the maximum and minimum normal stress on a material, while the von Mises directly visualizes the surface disruption magnitude while subjected to external forces and is not material property dependent.

5. Conclusions

A method for additively manufacturing mechanoluminescent samples by employing stereolithographic 3D printing was developed. Stress visualization and determination with an empirical method have immense potential in the rapid development phase of any production or construction process. The elimination of structural flaws in components or structural elements intended for industrial or civil applications has the potential to prevent design errors that would otherwise go unnoticed, given the complex nature of theoretical calculations. A complex 3D model was created, and theoretical stress distribution was calculated by COMSOL. The theoretical stress distribution during loading was compared to empirical measurements—the model was 3D printed with several finishing layers of ML powder, and the ML intensity was mapped during deformation. It was concluded that the empirical stress distribution obtained from a direct measurement method is in accordance with the calculated von Mises stress distribution and can therefore be improved for more complex technological uses. It was discovered that it is feasible to just apply ML powder to the top layers of the print for the sake of material conservation. The number of ML layers for the best ML contrast was found to be 10 layers. Future research into the appropriate ratio of ML particles to photopolymer has the potential to significantly reduce production costs even more.

This approach has the potential to be a valuable contribution to computational stress–strain analysis. It enables the real-time measurement of complicated unequal stresses on complex parts, resulting in a high commercialization potential.

Author Contributions: Conceptualization, A.S. and V.V.; methodology, E.E.; validation, A.Z. and V.V.; formal analysis, A.S. and E.E.; investigation, E.E. and A.S.; data curation, A.Z. and E.E.; writing—original draft preparation, E.E.; writing—review and editing, V.V., E.E. and A.S.; visualization, A.S. and E.E.; supervision, A.Z. All authors have read and agreed to the published version of the manuscript.

Funding: This work was supported by the European Regional Development Fund, grant number 1.1.1.1/20/A/138, 2021–2023. Institute of Solid State Physics, University of Latvia as the Center of Excellence has received funding from the European Union's Horizon 2020 Framework Programme H2020-WIDESPREAD-01-2016-2017-TeamingPhase2 under grant agreement No.739508, project CAMART2.

Data Availability Statement: The data presented in this study are available on request from the corresponding author.

Conflicts of Interest: The authors declare no conflict of interest.

References

1. Siripongpreda, T.; Hoven, V.P.; Narupai, B.; Rodthongku, N. Emerging 3D Printing Based on Polymers and Nanomaterial Additives: Enhancement of Properties and Potential Applications. *Eur. Polym. J.* **2023**, *184*, 111806. [CrossRef]
2. Ravi, P.; Burch, M.B.; Farahani, S.; Chepelev, L.L.; Yang, D.; Ali, A.; Joyce, J.R.; Lawera, N.; Stringer, J.; Morris, J.M.; et al. Utility and Costs During the Initial Year of 3D Printing in an Academic Hospital. *J. Am. Coll. Radiol.* **2022**, *20*, 193–204. [CrossRef] [PubMed]
3. Cheng, P.; Peng, Y.; Li, S.; Rao, Y.; le Duigou, A.; Wang, K.; Ahzi, S. 3D Printed Continuous Fiber Reinforced Composite Lightweight Structures: A Review and Outlook. *Compos. B Eng.* **2023**, *250*, 110450. [CrossRef]
4. Zarek, M.; Layani, M.; Cooperstein, I.; Sachyani, E.; Cohn, D.; Magdassi, S. 3D Printing of Shape Memory Polymers for Flexible Electronic Devices. *Adv. Mater.* **2016**, *28*, 4449–4454. [CrossRef] [PubMed]
5. Yang, H.; Leow, W.R.; Wang, T.; Wang, J.; Yu, J.; He, K.; Qi, D.; Wan, C.; Chen, X. 3D Printed Photoresponsive Devices Based on Shape Memory Composites. *Adv. Mater.* **2017**, *29*, 1701627. [CrossRef]
6. Liu, Y.; Zhang, F.; Leng, J.; Fu, K.; Lu, X.L.; Wang, L.; Cotton, C.; Sun, B.; Gu, B.; Chou, T.W. Remotely and Sequentially Controlled Actuation of Electroactivated Carbon Nanotube/Shape Memory Polymer Composites. *Adv. Mater. Technol.* **2019**, *4*, 1900600. [CrossRef]
7. Ze, Q.; Kuang, X.; Wu, S.; Wong, J.; Montgomery, S.M.; Zhang, R.; Kovitz, J.M.; Yang, F.; Qi, H.J.; Zhao, R. Magnetic Shape Memory Polymers with Integrated Multifunctional Shape Manipulation. *Adv. Mater.* **2020**, *32*, 1906657. [CrossRef]
8. Zhao, Z.; Wu, J.; Mu, X.; Chen, H.; Qi, H.J.; Fang, D. Desolvation Induced Origami of Photocurable Polymers by Digit Light Processing. *Macromol. Rapid Commun.* **2017**, *38*, 1600625. [CrossRef]

9. Chandra, B.P.; Shrivastava, K.K. Dependence of Mechanoluminescence in Rochelle-salt Crystals on the Charge-produced During Their Fracture. *J. Phys. Chem. Solids* **1978**, *39*, 939–940. [CrossRef]
10. Bünzli, J.C.G.; Wong, K.L. Lanthanide Mechanoluminescence. *J. Rare Earths* **2018**, *36*, 1–41. [CrossRef]
11. Terasaki, N.; Xu, C.-N.; Li, C.; Zhang, L.; Li, C.; Ono, D.; Tsubai, M.; Adachi, Y.; Imai, Y.; Ueno, N.; et al. Visualization of Active Crack on Bridge in Use by Mechanoluminescent Sensor. In Proceedings of the Health Monitoring of Structural and Biological Systems 2012, San Diego, CA, USA, 11–15 March 2012; SPIE: Bellingham, WA, USA; Volume 8348, p. 83482D.
12. Feng, A.; Smet, P.F. A Review of Mechanoluminescence in Inorganic Solids: Compounds, Mechanisms, Models and Applications. *Materials* **2018**, *11*, 484. [CrossRef] [PubMed]
13. Fujio, Y.; Xu, C.N.; Terasawa, Y.; Sakata, Y.; Yamabe, J.; Ueno, N.; Terasaki, N.; Yoshida, A.; Watanabe, S.; Murakami, Y. Sheet Sensor Using $SrAl_2O_4$: Eu Mechanoluminescent Material for Visualizing Inner Crack of High-Pressure Hydrogen Vessel. *Int. J. Hydrogen Energy* **2016**, *41*, 1333–1340. [CrossRef]
14. Ahn, S.Y.; Timilsina, S.; Shin, H.G.; Lee, J.H.; Kim, S.H.; Sohn, K.S.; Kwon, Y.N.; Lee, K.H.; Kim, J.S. In Situ Health Monitoring of Multiscale Structures and Its Instantaneous Verification Using Mechanoluminescence and Dual Machine Learning. *iScience* **2023**, *26*, 105758. [CrossRef] [PubMed]
15. Shin, H.G.; Timilsina, S.; Sohn, K.S.; Kim, J.S. Digital Image Correlation Compatible Mechanoluminescent Skin for Structural Health Monitoring. *Adv. Sci.* **2022**, *9*, 2105889. [CrossRef] [PubMed]
16. Jia, Y.; Yei, M.; Jia, W. Stress-Induced Mechanoluminescence in $SrAl_2O_4$: Eu^{2+}, Dy^{3+}. *Opt. Mater.* **2006**, *28*, 974–979. [CrossRef]
17. Liu, L.; Xu, C.N.; Yoshida, A.; Tu, D.; Ueno, N.; Kainuma, S. Scalable Elasticoluminescent Strain Sensor for Precise Dynamic Stress Imaging and Onsite Infrastructure Diagnosis. *Adv. Mater. Technol.* **2019**, *4*, 1800336. [CrossRef]
18. Jafari, A.; Broumand, P.; Vahab, M.; Khalili, N. An EXtended Finite Element Method Implementation in COMSOL Multiphysics: Solid Mechanics. *Finite Elem. Anal. Des.* **2022**, *202*, 103707. [CrossRef]
19. Sivakumar, N.; Kanagasabapathy, H.; Srikanth, H.P. Static Multiple, Distributed Piezoelectric Actuator Structural Deformation and Bending Analysis Using Comsol. *Mater. Today Proc.* **2018**, *5*, 11516–11525. [CrossRef]
20. Zhuang, Y.; Xie, R.J. Mechanoluminescence Rebrightening the Prospects of Stress Sensing: A Review. *Adv. Mater.* **2021**, *33*, 2005925. [CrossRef]
21. Kim, J.S.; Kwon, Y.N.; Shin, N.; Sohn, K.S. Mechanoluminescent $SrAl_2O_4$: Eu, Dy Phosphor for Use in Visualization of Quasidynamic Crack Propagation. *Appl. Phys. Lett.* **2007**, *90*, 241916. [CrossRef]
22. Einbergs, E.; Zolotarjovs, A. Programmable Material Testing Device for Mechanoluminescence Measurements. *HardwareX* **2022**, *12*, e00349. [CrossRef] [PubMed]
23. Einbergs, E.; Zolotarjovs, A.; Bite, I.; Vītola, V.; Spustaka, A.; Tunēns, G.; Arnautov, A. A Mechanoluminescence Based Approach to Spatial Mechanical Stress Visualisation of Additively Manufactured (3D Printed) Parts. *Materialia* **2022**, *24*, 101516. [CrossRef]
24. Azad, A.I.; Rahimi, M.R.; Yun, G.J. Quantitative Full-Field Strain Measurements by SAOED ($SrAl_2O_4$: Eu^{2+}, Dy^{3+}) Mechanoluminescent Materials. *Smart Mater. Struct.* **2016**, *25*, 095032. [CrossRef]
25. Rojas-Hernandez, R.E.; Rubio-Marcos, F.; Rodriguez, M.Á.; Fernandez, J.F. Long Lasting Phosphors: SrAl2O4: Eu, Dy as the Most Studied Material. *Renew. Sustain. Energy Rev.* **2018**, *81*, 2759–2770. [CrossRef]
26. Vitola, V.; Bite, I.; Millers, D.; Zolotarjovs, A.; Laganovska, K.; Smits, K.; Spustaka, A. The Boron Effect on Low Temperature Luminescence of $SrAl_2O_4$: Eu, Dy. *Ceram. Int.* **2020**, *46*, 26377–26381. [CrossRef]
27. Botterman, J.; Smet, P.F. Persistent Phosphor $SrAl_2O_4$: Eu, Dy in Outdoor Conditions: Saved by the Trap Distribution. *Opt. Express* **2015**, *23*, A868. [CrossRef]
28. Vitola, V.; Millers, D.; Smits, K.; Bite, I.; Zolotarjovs, A. The Search for Defects in Undoped $SrAl_2O_4$ Material. *Opt. Mater.* **2019**, *87*, 48–52. [CrossRef]
29. Doke, G.; Krieke, G.; Antuzevics, A.; Sarakovskis, A.; Berzina, B. Optical Properties of Red-Emitting Long Afterglow Phosphor Mg_2Si_1-XGexO_4: Mn^{2+}/Mn^{4+}. *Opt. Mater.* **2023**, *137*, 113500. [CrossRef]
30. Zhang, J.C.; Wang, X.; Marriott, G.; Xu, C.N. Trap-Controlled Mechanoluminescent Materials. *Prog. Mater. Sci.* **2019**, *103*, 678–742. [CrossRef]